Cureus Journal of Engineering

Open Access Original Article

Orbit Maneuvering of Vickay-1 Space Satellite Amidst Ionospheric Constraints Over Akure, Southwestern Nigeria

Ajobiewe K. Victor [1, 2] , Sola R. Fayose [2] , Seyi F. Olatoyinbo [3] , Nelson O. Ibigbami [4]

1. Space Physics, National Space Research and Development Agency, Abuja, NGA 2. Physics and Electronics, Adekunle Ajasin University Akungba Akoko, Ondo State, NGA 3. Mechanical Engineering, National Space Research and Development Agency, Abuja, NGA 4. Software Engineering, National Space Research and Development Agency, Abuja, NGA

Corresponding author: Ajobiewe K. Victor, vicajokayode@gmail.com

Received 05/15/2025
Review began 06/08/2025
Review ended 06/16/2025
Published 07/21/2025

DOI: https://doi.org/10.7759/s44388-025-06009-2

Abstract

The need to enhance the performance of the Vickay-1 space satellite in orbit amidst the impacts of the ionosphere constraints necessitated the design of the research work. The Vickay-1 space satellite in orbit monitored different levels of ionosphere constraints using ionosonde data over Akure, Southwestern Nigeria, over an average of 11 years (2011-2021) of the solar cycle. The study examined the impacts of ionospheric constraints such as troubled events like geomagnetic storms, coronal mass ejections, solar flares, solar wind, and sunspots on the paths of space satellite signal transmission using cross plots of the analyzed ionosonde data, and also determined to what extent to maneuver the space satellite orbit in order to overcome the troubled events.

The ionosonde data used in this study, namely geomagnetic field data, coronal mass ejection data, solar wind data, sunspot data, and solar flare intensity data as monitored by the Vickay-1 space satellite, were obtained from the National Oceanic and Atmospheric Administration. The data were processed and analyzed using MATLAB 2019 and Microsoft Excel. Cross-plots of the analyzed data were used to determine the different levels of the ionospheric constraints (high, moderate, and low) over Akure. Using Hohmann's transfer function, the orbit elements namely the inclination angle, altitude, total orbit energy, total orbit velocity and total orbit period of the Vickay-1 satellite were similarly determined to control its orbit against the ionospheric limitations.

Findings from this study indicated that the estimated values obtained from the cross plots ranged as follows: geomagnetic storm (6.69 to 8.45 kp), coronal mass ejection (1.59×10^{28} to 6.66×10^{29} MeV), solar wind velocity (345.97 to 465.35 km s^{-1}), sunspot number (46.22 to 50.45), and solar flare intensity (2.00×10^{-5} to 7.16×10^{-6} Watts m^{-2}). The determined orbit elements of the Vickay-1 space satellite showed inclination angle ranges from (82.5° to 262.5°), altitude (9583.69 to 30,454.67 km), total orbit energy (2.10×10^{-12} to 2.90×10^{-9} J), total orbit velocity (2.09×10^{-12} to 2.51×10^{-12} km hr^{-1}) and total orbit period (2.14×10^{-12} to 3.49×10^{-12} sec).

The study concluded that signal fading and multipath effects over Akure were caused by space satellite operational problems resulting from ionospheric constraints, and also proved that the orbit position of the Vickay-1 space satellite can be controlled from an altitude of approximately 9,583.69 km within the low earth orbit to an altitude of approximately 35,888.53 km between medium earth orbit and geosynchronous earth orbit to obtain efficient signal transmission over Akure. The study therefore, recommended that communication firms should identify the ionospheric impact conditions before adjusting their space satellite positions in order to improve low signal transmission challenges over Akure.

Categories: Space Engineering and Exploration, Telecommunication Networks, Wireless Communication Systems
Keywords: attenuation, transmission error, coronal mass ejection, geomagnetic storms, sunspot

Introduction

Radio waves traveling in the earth's atmosphere have many influence factors that affect them, as they propagates through the earth's upper ionosphere containing ionized gases or plasma. Solar parameters such as geomagnetic storm, sunspots, solar flare, coronal mass ejection (CME), and solar wind occurring at different timescales have implications on the path of radio wave transmission through the ionosphere [1-19]. These implicative factors are therefore referred to as the ionospheric constraints. It has been established that solar cycles undergo an 11-year periodic variation of solar magnetic field polarity activity. These periodic behavior influences variations of all solar parameters on different timescales ranging from days to years [4,12]. There have been several studies done to ascertain periodicities of different solar parameters. For instance, the 154-day periodicity of solar soft X-ray flare occurrence was studied and investigated on the basis of long-term solar flare activity and found that the smoothed monthly peak fluxes of C, M, and X solar flares have time lags of 1 month, 5 months, and 21 months, respectively [5-11,17] compared to sunspot numbers recorded during solar cycle 23. Additionally, studies [12-23] explored solar mechanisms using magnetic flux rope and sunspots connection with solar flares, coronal holes, green coronal line, large-scale eruptions like CME and other eruptive phenomena to understand the periodic variations of solar parameters.

Studies have shown that in some cases, communication distances are greatly extended, while in other cases, communication distances are greatly reduced or eliminated due to changes in the ionosphere layer. Thus, changes in the ionosphere can produce dramatic changes in the ability to communicate [24-33]. As a result of the presence of ions and electrons in the ionosphere, magnetic and electric fields are often deflected, thereby resulting in refraction and diffraction of radio waves along their transmission paths, thus resulting in transmission impairment, signal fading, and multipath. How far a radio wave signal will travel within the radio horizon is determined by the distribution of the radio refractivity.

Several researchers [34-49] have carried out studies on radio refractivity for different regions and climates using measured local meteorological data in Nigeria and other parts of the world. Their results showed that the local climate has a substantial influence on the radio refractivity and consequently on the transmitted radio signals. Similarly, researchers [50-52] studied the variation of radio field strength and radio horizon distance over a few stations in Nigeria and concluded that, as a result of variation in the meteorological parameters, hydrometeors such as rain, hail, snow, clouds, water vapor, and other gases in each geographical location, there is signal fading on the path of satellite signal transmission due to variation in the radio field strength over radio horizon distances in Nigeria. Hence, our study was necessitated to overcome these hydrometeors by examining, across an average of 11 years (2011-2021) of the solar cycle, the impacts of the ionospheric constraints on Vickay-1 space satellite performance in orbit and to devise means of maneuvering its orbit against such ionospheric impact conditions using Hohmann's transfer function.

Materials And Methods

This study investigated the average monthly values of each ionospheric constraints with respect to the solar activity, using ionosonde data obtained for a period of 11 years (2011-2021) of the solar cycle. Essential principles and terms of the solar space environments were examined in conjunction with computer-based software such as MATLAB 2019 and Microsoft packages. The ionosonde data used in this study composes of geomagnetic storm, coronal mass ejection, sunspot, solar flares, solar cycle, and solar wind data. The data set were obtained from both the National Aeronautics and Space Administration website and National Oceanic and Atmospheric Administration website. Parameters of Vickay-1 space satellite such as periapsis, apoapsis, inclination angle, eccentricity, mass, and period were archived through National Aeronautics and Space Administration website, to enhance determination of Hohmann's transfer orbit parameters for onward maneuvering process of Vickay-1 space satellite against the impacts of the ionospheric constraints.

Averages of the monthly data were computed to investigate the periodic variations and distributions of the ionospheric constraints. The average monthly data used in this study covered the years 2011-2021, as obtained in archived folders comprising of daily data prepared into text files by the United States Department of Commerce [35]. It is important to note that the average monthly data for a month is obtained simply by adding up all the data values for each day in that month and averaging the summed values.

The impacts of ionospheric constraints on the performance of Vickay-1 space satellite in orbit were critically examined via the ionospheric constraints classification, and the Hohmann's transfer function was equally employed to devise means of maneuvering its orbit against the ionospheric impact conditions for improved performance.

Ionospheric Constraints Classification (ICC)

The ICC was adopted and generally used to measure and predict each of the ionospheric constraints on the basis of their intensities and strength [17,20,32]. This would foster efficient and transient view of their impacts on space satellite signal transmission and efficiency as further explained below.

Geomagnetic storms could be classed with respect to their disturbance storm time index (Dst) in four categories [14]. Geomagnetic storm can be weak (Dst 50nT), moderate (-100nT Dst ≤ -50nT), intense (Dst ≤ -100nT), and severe (Dst ≤ -200 nT) while the geomagnetic disturbance index (Kp) (Table *1*) varies from weak (0 = Kp $\leq$5), moderate (5 Kp $\leq$6), strong (Kp = 7), severe (Kp = 8), and extreme (Kp = 9).

The CME which is often associated with solar radiation can be classed (Table *2*) with respect to the amount of solar radiation wavelength absorbed. Thus, research has shown [40] that the intensity of CMEs varies from minor (E $< 10^{28}$ MeV), moderate ($10^{28} <$ E $< 10^{29}$ MeV), strong ($10^{29} <$ E $< 10^{30}$ MeV), severe ($10^{30} <$E $< 10^{31}$ MeV), to extreme (E $\geq 10^{31}$ MeV) values in nature.

The modern classification system (Table *3*) for solar flares uses the letters A, B, C, M, or X, according to the peak flux in watts per square meter (Watts m^{-2}) of soft X-rays with wavelengths from 1 to 8 ångströms), as measured by the GOES spacecraft in geosynchronous orbit. X class flares are big; they are major events that can trigger planet-wide radio blackouts and long-lasting radiation storms. M class solar flares are medium-sized; they can cause brief radio blackouts. Studies [23,37] showed that each category for X-ray flares has nine subdivisions ranging from, e.g., C1 to C9, M1 to M9, and X1 to X9. M1 is 10 times stronger than C1. X1 is 10 times stronger than M1, and so on. The number provides more information about its strength.

Sunspots come in all sizes and shapes. They are classified with respect to the numbers in which they appear. Scientists have further classed their groupings on the basis of a more complex magnetic structure, which makes them more likely to produce solar flares [8]. Our major focus here is based on the number of sunspots that appear. Solar minimum is the point with the lowest number of sunspots, while solar maximum is the point at which the greatest number of sunspots appear.

The study [49] showed that solar wind exists in two fundamental states (Table 4) as slow solar wind and fast solar wind, each having a velocity of $\leq$350 km s^{-1}) and $\geq$450 km s^{-1}) and a temperature of $\geq$ 1.4 MK and $\leq$1.2 MK. The slow solar wind is twice dense and more variable in nature than the fast solar wind [26,46]. Observations of the Sun between 1996 and 2001 showed that emission of the slow solar wind occurred at latitudes up to \(30°) to \(35°) during the solar minimum (the period of lowest solar activity), then expanded toward the poles as the solar cycle approached maximum. At solar maximum, the poles were also emitting a slow solar wind [33]. The slow solar wind appears to originate from a region around the Sun's equatorial belt that is known as the "streamer belt" while the fast solar wind originates from coronal holes [49], which are funnel-like regions of open field lines in the Sun's magnetic field [21]. The solar wind affects other incoming cosmic rays interacting with planetary atmospheres. Moreover, planets with a weak or non-existent magnetosphere are subject to atmospheric stripping by the solar wind.

Scale	Description	Physical Measure (Kp)
G5	Extreme	Kp = 9
G4	Severe	Kp = 8
G3	Strong	Kp = 7
G2	Moderate	Kp = 6
G1	Minor	Kp = 5

TABLE 1: Classification of Geomagnetic Storms

Refer to the study in [53].

Coronal Mass Ejection Level	Energy of Coronal Mass Ejection (MeV)
L1	$E < 10^{28}$
L2	$10^{28} < E < 10^{29}$
L3	$10^{29} < E < 10^{30}$
L4	$10^{30} < E < 10^{31}$
L5	$E \geq 10^{31}$

TABLE 2: Classification of Coronal Mass Ejection Energy Levels

Refer to the study in [40,53].

Class	Peak (W/m^2) between 1 and 8 Angstroms
A	$I < 10^{-7}$
B	$I < 10^{-6}$
C	$10^{-6} <= I < 10^{-5}$
M	$10^{-5} <= I < 10^{-4}$
X	$I >= 10^{-4}$

TABLE 3: Classification of Solar Flares Intensity

Refer to the study in [53].

Type of Solar Wind Speed		Color in Figures		Solar Wind Speed (kms^{-1})		Temperature (T)	
Slow Solar Wind	Fast Solar Wind	Red	Blue	≤350	≥400	≥ 1.4 MK	≤ 1.2 MK

TABLE 4: Classification of Solar Wind

Refer to the study in [7].

Hohmann's Transfer Function (HTF)

Dr. Hohmann, a civil engineer, published his first seminal book and described optimal orbit transfer between two circular coplanar space orbits by numerical examples [47], and this transfer orbit is now generally called the Hohmann transfer. He further showed that an interplanetary trajectory requiring the least expenditure of energy is an ellipse tangent to the orbits of both the departure and arrival planets [47]. The Hohmann's transfer function (HTF) was employed to carry out accurate and reliable means of maneuvering Vickay-1 space satellite orbit. HTF operates with the use of an elliptical orbit termed the Hohmann's transfer orbit (HTO). This orbit is connected to the low earth orbit (LEO) at the point of perigee, which is the closest point forming a tangent and also connected to the geosynchronous earth orbit (GEO) at the point of apogee, which is the farthest point forming a tangent [13]. The advantage of the HTO is that it consumes the least possible amount of propellant. Space satellites, once in their mission orbits, need no additional orbit adjustment [13]. On the other hand, mission requirements may demand that we maneuver the satellite to correct the orbital elements when faced with perturbing events resulting from geomagnetic storms, CME, solar flares, solar maximum, solar minimum, and solar wind.

Using HTF entails launching a spacecraft and accelerating it across a series of alternate mission orbits until it moves to some final orbit at the end of its useful life. Each of these orbit changes requires energy [13]. The V budget is traditionally used to account for this energy. It sums all the velocity changes required throughout the space mission life. In a broad sense the V budget represents the cost for each mission orbit scenario. For HTF to be carried out successfully on Vickay-1 space satellite each of its parameters was extensively examined as outlined below.

The interval of time in which a spacecraft must be launched in order to complete its mission. For a satellite to be launched into an orbit, it requires an inclination angle i in an azimuth direction A_z

$$\sin A_z = \frac{\cos i}{\cos \Phi}$$

where Φ is launch site latitude, i is orbit inclination angle and A_z is launch azimuth direction. For a due east launch A_z is 90^0 and , hence the launch window is given by:

$$LW = \frac{2\Delta\pi}{w_e}$$

Where π is longitude of ascending node, w_e is Earth's rotation rate and $\Delta\pi$ is $w_e t$, $\Delta\pi$ is termed maximum permissible nodal increment with plane change angle ξ required to transfer from launch orbit plane to the mission orbit plane.

$$\xi = \arccos(\cos^2 i) + \sin^2 i \cos \Delta\pi$$

Any two body of mass m_1 and m_2 with distance r apart are attracted to each other with a force:

$$F = G\frac{m_1 m_2}{r^2}$$

where G is constant of gravitation given as (6.6726 + 0.0005) × 10^{-11} m^3 kg s^{-2}. $+G$ indicates motion toward earth while the $-G$ demonstrates any motion farther from the earth station.

$$\mu = GM_e$$

μ is a universal constant of gravitation, M_e is Earth's mass. For a gravitational potential

$$F = \bigtriangledown V$$

$\bigtriangledown$ is the gradient and V is gravitational potential. For a spherical body,

$$V = \frac{\mu}{r}$$

For non-spherical body, V, contains additional terms that can be used to determine energy

$$\frac{\dot{r}^2}{2} - \frac{\mu}{r} = \xi$$

The above equation is used to determine the specific mechanical energy of the satellite where $\frac{\dot{r}^2}{2}$ is Specific kinetic energy of the satellite and - $\frac{\mu}{r}$ is Specific potential energy of the satellite.

This has to do with the property of the satellite in motion as it relates to the product of the moment of inertia and the angular velocity of the satellite in orbit.

$$H^2 = \mu r + rB\cos\Theta$$

H is angular momentum of satellite and B is constant of integration, r for orbit maneuvering

$$r = \frac{\frac{H^2}{\mu}}{1 + (B \ldots}$$

where $\frac{H^2}{\mu}$ is P known as semilatus rectum, $\frac{B}{\mu}$ is e which is the eccentricity also taken as $\frac{(1 + 2\xi H^2)^{\frac{1}{2}}}{\mu^2}$ and Θ is the true anomaly. Thus,

$$r = \frac{P}{1 + e\cos\Theta}$$

This explains the various principles taken to attain the trajectory paths for space orbit maneuvering processes of a satellite in orbit.

semimajor axis is $a = \frac{r_a + r_p}{2}$

semiminor axis is $b = a\sqrt{1 - e^2}$

eccentricity is $e = \frac{r_a - r_p}{r_a + r_p}$

r_a is apogee or farthest radius to the satellite given as $a(1 + e)$, while r_p is perigee or closest radius to the satellite given as $a(1 - e)$

$$P = a(1 - e^2) = \frac{b^2}{a} = r_p(1 + e) = r_a(1 - e)$$

γ = flight - path angle

$$\gamma = \frac{\pi}{2} - \beta$$

Radial Velocity Component is $V_r = \sqrt{\frac{\mu}{p}} e\sin\Theta$

Normal Velocity Component is $V_n = \sqrt{\frac{\mu}{p}}(1 + e\cos\Theta)$

Flight Path Angle is : $\gamma^0 = \arccos\frac{V_n}{V} = \arctan\frac{V_r}{V_n}$

Where V given as $(V_n^2 + V_r^2)^{\frac{1}{2}}$

Perigee Velocity is $V_p = \sqrt{\frac{\mu}{p}}(1 + e)$

Apogee Velocity is $V_a = \sqrt{\frac{\mu}{p}}(1 - e)$

Energy ξ at any point in orbit is $\xi = \frac{V^2}{2} - \frac{\mu}{r}$

As $e \rightarrow 1, V_a \rightarrow 0, r_a \rightarrow 2a$ then,

$$\xi = -\frac{\mu}{2a}$$

$$V = \sqrt{\mu(\frac{2}{r} - \frac{1}{a})}$$

For a circular orbit, $V_c = \sqrt{\frac{\mu}{r}}$

For escape trajectory, $a \rightarrow \infty, V_{esc} = \sqrt{2V_c}$

V_c is circular orbit velocity and V_{esc} is escape velocity

Period of Elliptic Orbit is $P = \frac{2\pi}{n}, where n = \sqrt{\frac{\mu}{a^3}}$

The ΔV budget is used to carry out the orbit maneuvering process of Vickay-1 satellite and is therefore calculated by comparing the initial and final orbit velocity vectors as well as the inclination plane change required [45]. We investigate two types of maneuvers using bi-elliptical transfer orbits.

$$V = \sqrt{\mu[\frac{2}{r} - \frac{1}{a}]}$$

V is magnitude of orbit velocity at some point, r is magnitude of the radius from the focus to that point, a is semi major axis of the orbit, and μ is gravitational constant of the attracting body.

Re-arranging the above equation gives,

$$V^2 = \mu[\frac{2}{r} - \frac{1}{a}]$$

$$\frac{V^2}{2} = \frac{\mu}{r} - \frac{\mu}{2a}$$

$$\frac{V^2}{2} - \frac{\mu}{r} = -\frac{\mu}{2a}$$

$$\frac{kineticenergy}{satellitemass} + \frac{potentialenergy}{satellitemass} = \frac{totalenergy}{satellitemass}$$

The total energy is dependent only on a, as a increases energy increases.

By comparison ξ is the total energy of an orbiting satellite, thus

$$\xi = -\frac{\mu}{2a}$$

Plotting $\xi = -\frac{\mu}{2a}$ against $P = \frac{2\pi}{\sqrt{\mu}} a^{\frac{3}{2}}$ gives the lowest energy and period points corresponding to the space satellite parking orbit.

Recall from the energy equation that, $V^2 = \mu[\frac{2}{r} - \frac{1}{a}]$

$$V_{cl}^2 = \frac{\mu}{r_1}$$

V_{cl} is the circular velocity, thus for the first orbit

$$V_1^2 = \frac{\mu}{r_1}[2 - \frac{2}{1 + \frac{r_f}{r_1}}]$$

Since, $2a = r_1 + r_2 = r_1(1 + (\frac{r_f}{r_1}))$

$$V_{1^2} = V_{cl}^2[\frac{2 + 2(\frac{r_f}{r_1}) - 2}{1 + (\frac{r_f}{r_1})}]$$

$$\frac{V_1}{V_{cl}} = \sqrt{\frac{2(\frac{r_f}{r_1})}{1 + (\frac{r_f}{r_1})}}$$

$$\frac{\Delta V_1}{V_{cl}} = \frac{V_1 - V_{cl}}{V_{cl}} = \sqrt{\frac{2(\frac{r_f}{r_1})}{1 + (\frac{r_f}{r_1})}} - 1$$

$$V_1^2 = \frac{\mu}{r_1}[2 - \frac{2}{1 + (\frac{r_f}{r_1})}]$$

$$V_f^2 = \frac{\mu}{r_f}[2 - \frac{2}{1 + (\frac{r_f}{r_1})}]$$

$$V_f^2 = \mu[\frac{2}{r_f} - \frac{2}{r[1 + (\frac{1}{\frac{r_f}{r_1}})]}]$$

$$r_1 + r_f = r_f(1 + \frac{1}{\frac{r_f}{r_1}})$$

$$V_f^2 = \frac{\mu}{r_f}[2 - \frac{2(\frac{r_f}{r_1})}{1 + (\frac{r_f}{r_1})}]$$

Hence since, is $\frac{\mu}{r_1}$, similarly V_{cf}^2 is $\frac{\mu}{r_f}$

$$V_{cf}^2 = V_{cl}^2 \frac{r_1}{r_f}$$

$$V_f^2 = V_{cf}^2[\frac{2 + 2(\frac{r_f}{r_1}) - 2(\frac{r_f}{r_1})}{1 + (\frac{r_f}{r_1})}]$$

$$V_f^2 = \frac{V_{cl}^2}{\frac{r_f}{r_1}}[\frac{2}{1 + (\frac{r_f}{r_1})}]$$

$$\frac{V_f}{V_{cl}} = \sqrt{\frac{2}{\frac{r_f}{r_1}[1 + (\frac{r_f}{r_1})]}}$$

$$\frac{\Delta V_f}{V_{cl}} = \frac{V_{cf} - V_f}{V_{cl}} = \sqrt{\frac{1}{\frac{r_f}{r_1}}} - \sqrt{\frac{2}{\frac{r_f}{r_1}[1 + (\frac{r_f}{r_1})]}}$$

$$\frac{\Delta V_{Total}}{V_{cl}} = \frac{\Delta V_1}{V_{cl}} + \frac{\Delta V_f}{V_{cl}}$$

$\Delta V_{Total} = \Delta V_1 + \Delta V_f$ = Hohmann's Transfer Function

For a Bi-elliptic orbit transfer we considered the following sets of equations,

$$\frac{\Delta V_1}{V_{cl}} = \frac{V_1 - V_{cl}}{V_{cl}} = \sqrt{\frac{2(\frac{r_2}{r_1})}{1 + (\frac{r_2}{r_1})}} - 1$$

$$\frac{\Delta V_2}{V_{cl}} = \sqrt{\frac{2(\frac{r_f}{r_1})}{\frac{r_2}{r_1}[(\frac{r_2}{r_1}) + (\frac{r_f}{r_1})]}} - \sqrt{\frac{2}{\frac{r_2}{r_1}[1 + (\frac{r_2}{r_1})]}}$$

$$\frac{\Delta V_3}{V_{cl}} = \sqrt{\frac{2(\frac{r_2}{r_1})}{\frac{r_f}{r_1}[(\frac{r_f}{r_1}) + (\frac{r_2}{r_1})]}} - \frac{1}{\frac{r_f}{r_1}}$$

It is important to note that r_1 is the radius of the initial orbit while r_2 is the apogee radius of the second orbit, and r_f is the final circular orbit radius. Combining the last three equations above gives rise to the equation below, which is also known as Hohmann's bi-elliptic transfer function. It was used for the maneuvering process of the Vickay-1 satellite in orbit.

$$\Delta V_{Total} = \Delta V_1 + \Delta V_2 + \Delta V_f$$

Results

The averaged computed values (Tables 5-9) for each of the ionospheric constraints were carried out across the 11 years (2011-2021) of the solar cycle. It was observed that the highest value of the geomagnetic storm index is (8.45 Kp) while its lowest value is approximately (6.69 Kp). The average value of the number of sunspots across the 11-year solar cycle ranges from 46.21818 to 50.45455 in value. Also, the solar wind velocity of the streamed electrons emanating from the sun's coronal region ranges in value from 345.9677 km s^{-1} to 465.3548 km s^{-1}. The average solar flare intensity ranges from its lowest value at 2.00 × 10^{-5} watts m^{-2} to its highest value at 7.16 × 10^{-6} watts m^{-2}. Similarly, the coronal mass ejection data varied from 1.59 × 10^{28} MeV to 6.66 × 10^{28} MeV. These values (Tables 5-9) were plotted (Figures 1-5) to see how they affect Vickay-1 space satellite performances in orbit, in order to mitigate measures where appropriate by maneuvering its orbit against the ionospheric impact conditions.

Months	2011	2012	2013	2014	2015	2016	2017	2018	2019	2020	2021	Average Kp
1	5.5	7	7.6	5	9.5	9	10	5.6	6	4	4.4	6.690909
2	6	7.8	5.7	8	9.7	10	9.5	5.9	6	5	6.8	7.309091
3	6.7	11	7.4	7	12	10	10	6.6	6	5	8	8.154545
4	7.2	11	6.9	7	12	10	11	6.7	6	5	8.1	8.263636
5	7.6	9.8	7.5	7	11	10	11	6.8	6	5	7.8	8.136364
6	7.7	9.9	8.3	7	11	10	9.9	6.8	6	5	7.4	8.090909
7	7.7	10	8.5	6	11	10	9.7	6.6	6	5	7.1	7.963636
8	7.7	10	8.5	7	11	10	9.9	6.9	6	5	7	8.090909
9	8.2	9.8	8.1	7	12	10	11	7.1	6	5	7	8.290909
10	8.1	9.8	8.1	7	12	11	11	7	7	5	7	8.454545
11	7.8	9.6	7.8	7	12	11	11	6.9	6	5	7.3	8.309091
12	7.5	9.1	7.6	8	12	10	10	6.9	6	5	7.2	8.118182

TABLE 5: Average Geomagnetic Storm Index (Kp) Value

Months	2011	2012	2013	2014	2015	2016	2017	2018	2019	2020	2021	Average Spot
1	27	94	96	117	93	57	26	7	8	6	10	49.18182
2	37	72	79	131	81	57	26	9	4	3	9.4	46.21818
3	81	77	79	130	72	56	23	7	6	3	12	49.63636
4	58	79	86	126	73	51	26	7	7	3	15	48.27273
5	58	83	93	123	76	51	24	8	8	3	16	49.36364
6	57	84	90	120	74	46	23	10	6	3	18	48.27273
7	59	87	90	117	73	44	23	8	6	4	20	48.27273
8	59	88	90	116	72	45	24	8	5	4	20	48.27273
9	66	88	86	117	73	45	26	8	5	4	24	49.27273
10	72	87	89	114	72	44	25	8	4	5	25	49.54545
11	78	87	91	113	71	42	23	7	4	7	26	49.90909
12	81	85	94	113	70	40	22	7	4	9	30	50.45455

TABLE 6: Average Sunspot Value

Months	2011	2012	2013	2014	2015	2016	2017	2018	2019	2020	2021	Average Solar Flare
1	0.06	2.602	0.37	3	3.308	0.44	0.44	0.02	0.04	0.01	0.1	0.92
2	0.74	0.26	0.39	9.427	2.63	1.539	0.24	0.18	0	0	0.13	1.41
3	1.755	4.258	0.49	4.198	3.899	0.17	0.46	0.04	0.53	0	0.06	1.44
4	3.305	1.598	2.702	2.187	2.987	0.76	1.26	0.03	0.03	1.285	0.63	1.52
5	0.76	3.013	4.07	3.353	2.819	0.98	0.37	0.05	0.41	0	1.48	1.57
6	1.34	3.188	1.6	4.133	3.878	0.2	0.52	0.11	0	0.02	0.22	1.38
7	2.906	11.15	2.452	3.675	1.702	1.92	1.733	0	0	0	0.36	2.35
8	3.654	3.188	1.854	5.903	4.213	0.85	2.114	0	0	0.06	0.94	2.07
9	8.433	1.71	0.67	5.505	4.152	0.69	7.455	0	0	0	1.04	2.7
10	1.57	0.84	5.585	17.005	1.58	0.12	0.01	0.01	0	0.46	1.44	2.6
11	2.485	1.572	2.33	8.198	2.731	0.26	0	0	0	1.08	0.46	1.74
12	1.36	0.24	2.007	9.745	2.465	0.11	0	0	0	0.46	1.54	1.63

TABLE 7: Average Solar Flare Values

Months	2011	2012	2013	2014	2015	2016	2017	2018	2019	2020	2021	Average CME
1	5.41E+29	6.07E+29	3.82E+29	7.18E+29	2.42E+29	9.94E+29	5.88E+29	4.15E+29	6.26E+28	1.66E+28	0	1.57E+29
2	3.31E+29	7.94E+29	5.8E+29	3.67E+29	4.3E+29	3.46E+29	2.27E+29	3.28E+29	1.7E+29	3.58E+28	0	8.25E+28
3	6.97E+29	6.98E+29	3.84E+29	5.41E+29	3.67E+29	5.57E+29	5.12E+29	3.84E+29	6.66E+28	2.24E+28	0	2.41E+29
4	3.9E+29	8.07E+29	4.06E+29	6.14E+29	6.06E+29	1.69E+29	2.04E+30	5.31E+29	2.47E+29	3.06E+28	0	4.74E+28
5	3.41E+29	7.36E+29	9.34E+29	5.41E+29	5.47E+29	3.05E+29	2.55E+29	4.34E+29	6.07E+29	6.84E+28	0	6.58E+28
6	4.41E+29	9.01E+29	1.47E+30	5.71E+29	1.61E+30	1.58E+29	1.11E+30	6.37E+29	6.32E+28	4.72E+28	0	1.03E+29
7	7.21E+29	9.46E+29	4.98E+29	3.17E+29	3.76E+29	3.17E+29	9.18E+29	4.39E+29	7.47E+28	2.24E+29	0	6.66E+29
8	4.56E+29	5.16E+29	5.78E+29	2.68E+29	6.25E+29	1.39E+29	4.82E+29	3.24E+29	6.19E+28	1.18E+29	0	4.22E+28
9	8.32E+29	2.97E+29	5.33E+29	3.87E+29	9.43E+29	4.95E+29	1.15E+30	4.73E+29	8.57E+27	8.37E+28	0	5.57E+28
10	3.99E+29	2.78E+29	5.73E+29	3.38E+29	1.37E+30	1.59E+30	1.08E+30	5.89E+29	3.7E+28	2.31E+29	0	6.22E+28
11	6.36E+29	3.43E+29	4.79E+29	6.03E+29	9.39E+29	4.66E+29	3.39E+29	4.02E+29	2.17E+28	1.89E+29	0	1.59E+28
12	7.4E+29	2.63E+29	4.61E+29	3.32E+29	7.99E+29	1.97E+29	8.28E+28	3.13E+29	4.18E+28	2.16E+29	0	1.28E+29

TABLE 8: Average Coronal Mass Ejection (CME) Values

Months	2011	2012	2013	2014	2015	2016	2017	2018	2019	2020	2021	Average Solar Wind
1	412.2258	406.7478	365.2580	421.9032	413.3870	427.7096	485.58064	395.6451	406.2580	366	366.4516	413.8064
2	403.3214	411.6955	365.5	413.0357	410.9642	402.4482	471.4642	398.4285	411.8928	400.6896	436.2857	414.6206
3	426.4516	431.0909	417.4838	381.0322	473.5483	440.4838	504.8064	406.5161	387.1290	398.1290	441.0645	465.3548
4	441.4	407.1848	367.9	400.5666	422.8666	407.2	464.8333	394.6333	382.6	380.5333	417.6	398.9
5	445.7741	404.8005	448.4516	355.6129	402.3225	460.6451	414.1935	416.9354	394.9354	323.4516	383	407.4838
6	456.0333	411.3848	448.7333	379.9	454.6333	452	400.3333	424.9666	345.9333	339.9666	387.4666	435.2666
7	462.7419	411.7829	402.1290	337.4193	422.4838	456.7096	452.8064	399.2580	390.3548	358.5806	391.6129	455.5161
8	442.7741	422.7008	437.6129	361.1612	451.8387	446.5806	466.7096	422.7096	434.7096	388.1612	371.9032	425.5483
9	434.1666	431.3636	393.8666	421.4333	455.2666	462.9	515.2	433.7666	460.0666	405.1333	382.8	380.4
10	383.4516	406.6839	371.3125	396.0967	435.5161	488.3548	433.2258	405.7419	415.5806	390.2903	371.4687	382.48387
11	371.4333	406.8484	376.1666	437.0333	430.6333	438.5333	425.4333	402.6333	377.6666	379.1666	465.1333	371.5
12	362.2903	413.0910	362.6333	476	472.2258	469.8064	421.6451	436.6129	364.6774	402.7419	429.4	345.9677

TABLE 9: Average Solar Wind Values

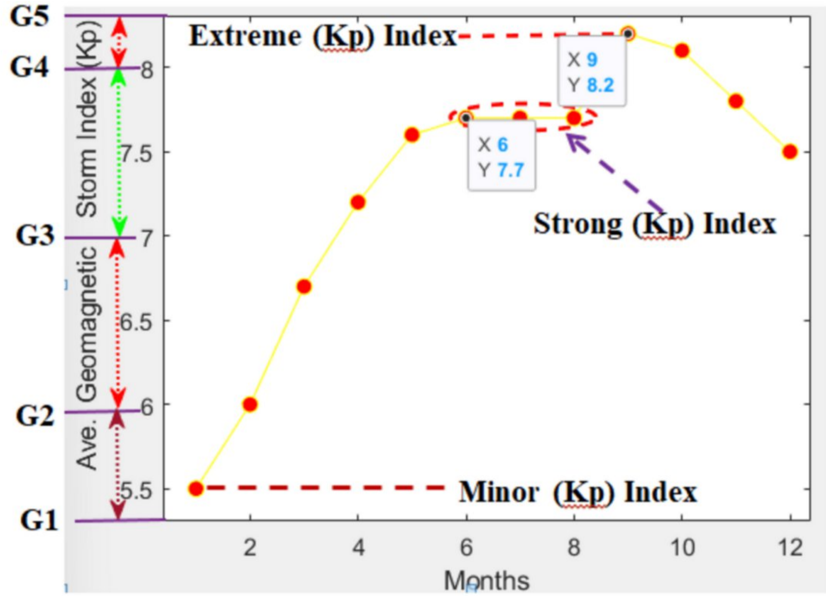

FIGURE 1: Average Geomagnetic Storm Index Constraint Against Months of Years (2011-2021)

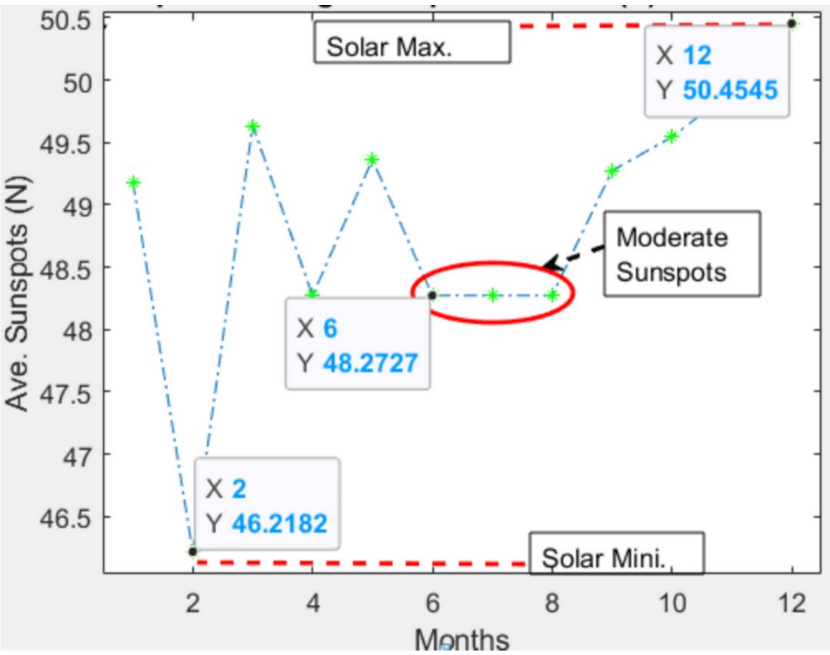

FIGURE 2: Average Sunspot Constraint Against Months of Years (2011-2021)

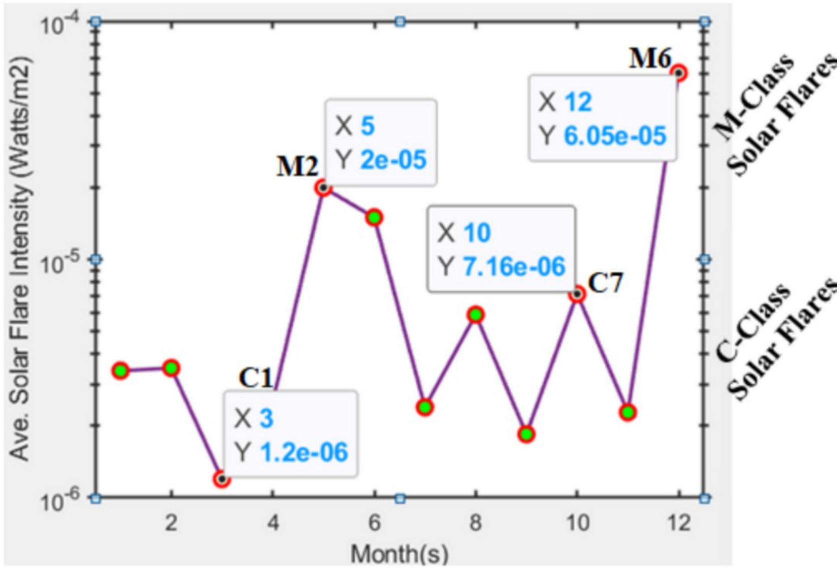

FIGURE 3: Average Solar Flares Constraint Against Months of Years (2011-2021)

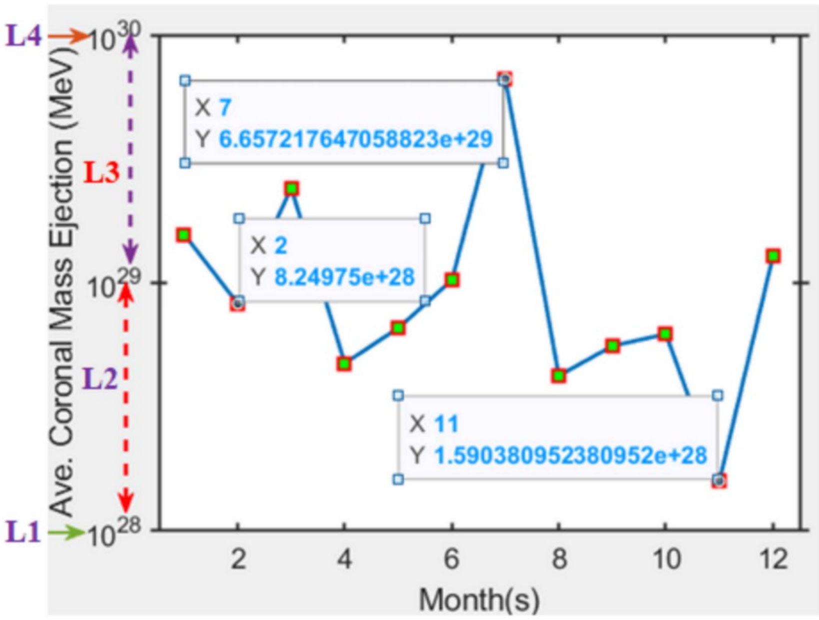

FIGURE 4: Average Coronal Mass Ejection (CME) Constraint Against Months of Years (2011-2021)

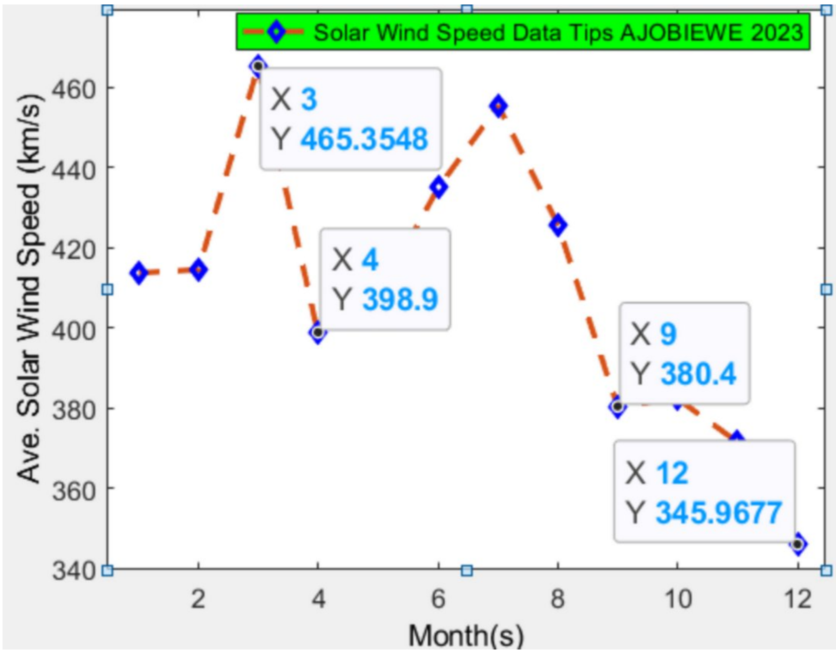

FIGURE 5: Average Solar Wind Speed Constraint Against Months of Years (2011-2021)

Vickay-1 space satellite was explicitly studied with respect to the observed ionospheric impact conditions. The satellite was launched at a space spot center to a LEO with an inclination angle of 82.50° to an altitude of approximately 9,583.69 km. The satellite while operating within the LEO orbit was seen having perigee and apogee radius of 249.5 km and 270 km, respectively, while its semi-major and semi-minor axis were 259.75 km and 259.72 km, respectively. Orbit parameters (Table 10) such as the radial velocity (V_r), Normal component velocity (V_n), flight path angle (γ), perigee velocity (V_p), and Apogee Velocity (V_a) of Vickay-1 satellite were determined in order to know the total orbit energy and total orbit velocity that would be needed to carry out its maneuvering process. To effectively achieve this orbit maneuver, we equally determined the Hohmann's orbit parameters (Table 11) for each of orbits 1, 2, and 3.

Mass	Eccentric (e)	Perigee (km)	r_p (km)	Apogee (km)	r_a (km)	Alti. (km)	Inc. Angle	a (km)	b (km)	V_r (km)	V_n (km)	γ^0	V_p (km/hr)	V_a (km/hr)
2260	0.00297	499	249.5	540	270	9583.69	82.5	259.75	259.72	7.09E-05	2.41E-03	1.68	2.42E-06	2.40E-06
2260	0.00297	61608.64	30804.32	61964.36	30982.18	20,080.93	172.5	30893.25	30887.1	8.57E-04	2.20E-03	75.62	2.22E-03	2.20E-03
2260	0.00297	71731.34	35865.67	72145.5	36072.75	30,454.67	262.5	35969.21	35965.61	-6.08E-15	2.05E-12	-0.2	2.06E-12	2.04E-12

TABLE 10: Estimated Orbit Parameters

Total Orbit Energy (ϵ)	Orbit Period (sec.)	Escape Velocity (V_{esc}) km/hr	Circular Velocity (V_{cl}) km/hr	Total Orbit Velocity (ΔV_{nT}) km/hr	Transfer Time (T_r) (sec)
2.90E-09	2.14E+12	1.01E-11	2.41E-12	2.51E-12	1.41E+12
2.40E-12	2.78E+15	3.10E-12	2.21E-12	2.09E-12	1.59E+12
2.10E-12	3.49E+15	2.90E-12	2.05E-12	2.26E-12	1.78E+12

TABLE 11: Hohmann's Orbit Parameters

A plot of the calculated total orbit energy (ξ) against the orbit period shown in (Figure 6) gives an interception point that predicts the parking altitude which should be between an altitude of 3×10^4 km and 4×10^4 km lying between medium earth orbit (MEO) and GEO as depicted in Figure 7. An altitude of 35,888.5332 km is precisely the most convenient parking altitude because the higher the satellite parking altitude, the better the signal coverage.

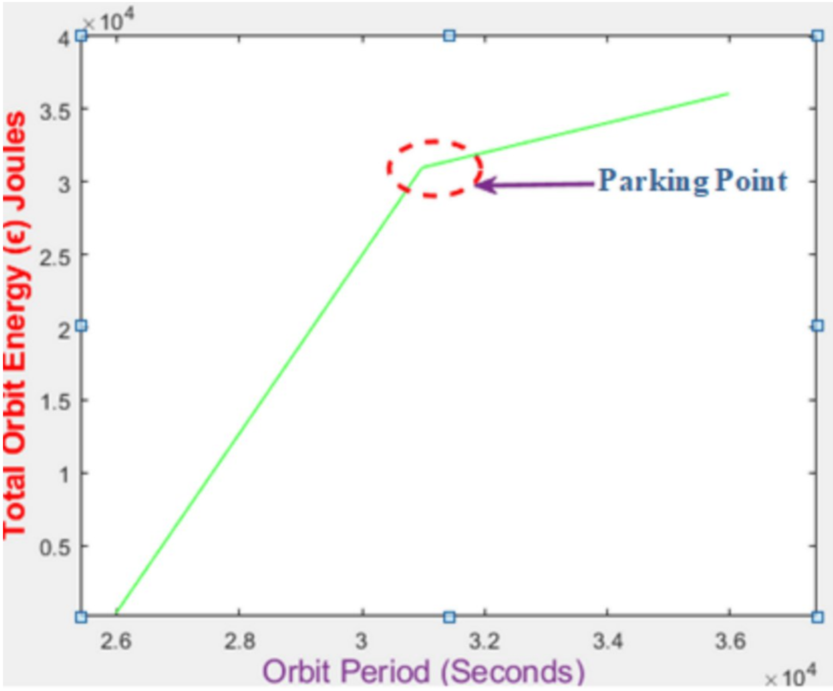

FIGURE 6: Vickay-1 Satellite Parking Orbit

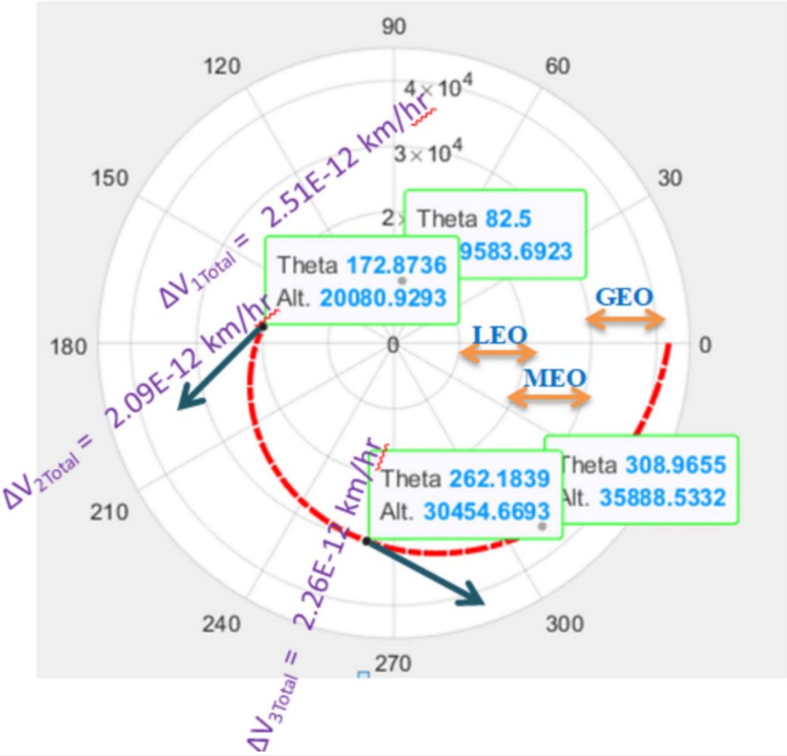

FIGURE 7: Hohnmann's Transfer of Vickay-1 Satellite

MEO, medium earth orbit; GEO, geosynchronous earth orbit; LEO, low earth orbit

Discussion

Figure 1 depicts the plot of the average geomagnetic storm index values (Table 5) obtained across the 11 years of the solar cycle. The averaged Kp index values were plotted against the months in order to classify their average values on the basis of minor, moderate, strong, severe, and extreme impact conditions represented as G1, G2, G3, G4, and G5, respectively. The morphology of the graph (Figure 1) showed a consistent and moderately steady rise in Kp index value. While the minor G1 level exists at 5.55 Kp, the moderate is said to be seen between G2 to G3 having 6 Kp to 7 Kp index. Satellites within these regions are subject to little drag and moderate or minor signal fading transmission might occur. However, a steady and strong geomagnetic storm index was observed at 7.7 Kp which is between G3 and G4. This period lies between June and August. The extreme geomagnetic storm index was staged at 8.2 Kp index between G4 and G5. The reason attributed to this is due to the increased surface charge on the satellite electronic components, creating sporadic intermittent satellite navigation, orientation, and tracking problems due to increased drag.

The second constraint under consideration has to do with the number of sunspot seen across the 11 years of the solar cycle. It was observed that the highest number of sunspot counts was taken as solar maximum, while that of the lowest sunspot count was taken as solar minimum. This study has helped to unveil the highest and lowest points of sunspot count across the 11 years of the solar cycle from the average data obtained (Table 6). Figure 2 displays a plot of the average sunspot data (Table 6) against the months. It was observed that the highest count of sunspots exists at 50.4545 and that of the lowest count exists at 46.2182. Thus, solar maximum and solar minimum exist at these points, respectively. However, the number of sunspots seen as 48.2727 shows a moderate and steady increase in value between the months of June and August across the 11 years of the solar cycle. It was also discovered that there was an undulating variance in value of the number of sunspots within the period of January to May. This inconsistent rise and decrease in value are as a result of the variance in the activity of the sun and most importantly as a result of the variance in the intensity of the sun's core activity. It is worthwhile to note that the moderate and steady rise in the number of sunspot count as stated earlier have adverse effect as most of the electronic components or solar panel of the space satellite could be obviously affected or burnt due to overcharging. Thus, the satellites must be clearly examined to avoid wreckage and signal fading.

One of the major factors also confronting satellite transmission performances is the solar flares. They are as a result of intense outburst of radiation released from the sun's surface. Mechanisms associated with flare eruptions have been studied by several authors [9-10,22,27,34,43,44] using soft X-ray techniques to show flux in B and C class flares. This study unveiled how the satellite data transmission is disrupted with respect to the radiative influence of the solar flare intensity. Figure 3 depicts a plot of the average solar flare intensity values (Table 7) against the months across the 11 years of the solar cycle. The letters A, B, C, M, or X were used (Table 3) to depict their variance across an average value of a complete solar cycle.

The only class of solar flares seen were that of class "C and M", whereas classes A, B, and X were absconded due to the set of available data within the period of the solar cycle. Class C though with least adverse effect to class M solar flares can result into radiation storms which often lead to transmission impairment that affect space satellite signal transmission. It was observed that they occur at an average range of values between 1.2×10^{-6} watts m^{-2} to 7.16×10^{-6} watts m^{-2} within the months of early January to late April, and later seen during the month of July to November with a consistent, steady and moderate value of 7.16×10^{-6} watts m^{-2}. The observed classes of C solar flares are that of C1 and C7, with C7 being the strongest to that of C1, the number provides more information about its strength. However, class M solar flare were seen between the periods of May to June at an average value of 2×10^{-5} watts m^{-2} and later seen within the month of December at 6.05×10^{-5} watts m^{-2}. M class solar flares are medium-sized solar flares that can cause radio blackouts which affect and disrupt satellite signal transmission. Therefore, it is well noted that within the period of June to August most space satellite signal performances could be well affected by solar flare intensity resulting from the sun's solar activity. The observed classes of M solar flares are that of M2 and M6, with M6 being the strongest to that of M2. This implies that the M class solar flares seen across the 11 years solar cycle are six times stronger in the month of December while that of C class solar flares seen are seven times stronger within the months of July to November.

Another important factor under consideration was the CME, which are huge bubbles of highly charged energetic plasma from the sun's corona that often produce geomagnetic storms posing hazards to space satellite operations. As a CME enters interplanetary space, it is capable of reaching and colliding with the earth's magnetosphere to form an interplanetary coronal mass ejection that damage space satellites through the release of a high current discharge penetrating its electronic components. The average CME data (Table *8*) was plotted against the months (Figure *4*) to depict the various energy levels (Table *2*) of the accompanying CME discharge across the 11 years of the solar cycle. It was observed that the only energy levels seen were that of L2 and L3, while energy levels L1, L4, and L5 were absconded due to the solar activity of CME across the average solar cycle. From the graph, CME was seen to be at the highest peak between the months of June and August with an average energy level of L3 having an approximate 6.6572×10^{29} MeV. This indicates a very strong energy level impact. Thus, within this period there could be an increased charging on the space satellite solar panel or micro ships which of course would cause interruption in receiving a better signal transmission. The energy level L2 of the CME depicted showed an approximate average energy value of 8.2498×10^{28} MeV between February and May and 1.5904×10^{28} MeV between very late August and November. This shows an undulating rise in the CME values due to the amount of plasma bubbles being released from the Sun's corona. These undulating rise and fall has a minor impact on the space satellite performance compared to that of L3 with a very strong impact.

Furthermore, the solar wind, which is a continuous stream of protons and electrons from the sun's outer atmosphere known as the corona, when strong enough would cause geomagnetic storms which invariably could wreak havoc on space satellite performance in orbit and threaten astronauts in space. It equally can lead to auroras expanding close to the equator during space weather conditions. Average solar wind speed data (Table *9*) was plotted against the months (Figure *5*) across the 11 years of the solar cycle. The solar wind speed was classified on how fast or slow (Table *4*) they emanate from the sun's corona. It was observed that the solar wind speed was slowest between the months of November to December with a steady decrease in value to approximately 345.97 km s^{-1}. This is as a result of the least solar activity within the nucleus of the sun's core, thereby leading to little decrease in the release of streamed protons and electrons from the corona. This would pose little or no threat to space satellite performance as little or no geomagnetic storms were formed. A close look at the graph shows the solar wind speed is fast but quiet undulating within the month of March with an approximate value of 465.35 km s^{-1}, whereas it exhibited consistent and steady rise in value between the months of April and August with an average value of approximately 398.9 km s^{-1} to above 458 km s^{-1}. This implies that within the said period there was steady and enormous release of streamed electrons and protons from the sun's core which invariably could result in the steady creation of geomagnetic storm and aurora that would cause a threat to the space satellite performance in orbit.

Therefore, it is worth noted that between the period of June and August of the solar cycle, performance of Vickay-1 satellite in orbit could be obviously affected due to the imposed threats received from the ionospheric constraints and it is deemed necessary to accord statutory maneuvers of its orbit to prevent malfunctioning and fading in the course of operation.

The values of Table *11* along with the orbit parameters (Table *10*) were used to carry out the orbit maneuvering of Vickay-1 space satellite against the ionospheric impact conditions. The polar plot (Figure *7*) depicts the exact altitude to which the satellite can be positioned to overcome the ionosphere constraints encountered in the cause of operation. From the polar plot (Figure *7*), it can be seen that the total orbit velocity change ($\Delta V_1, \quad \Delta V_2, \quad \Delta V_3$) at every maneuvering points were added tangentially to the eccentric orbit in order to attain the next desired altitude. Thus, this has help to show that Vickay-1 space satellite, which was subjected to ionospheric impact conditions while operating in orbit, at an altitude of approximately 9,583.69 km can be maneuvered twice to an altitude of approximately 35,888.53 km to overcome the ionospheric constraints. However, the differences in the values of each of the total velocity changes were as a result of the differences in both the gravitational constant and altitude in the cause of maneuvering.

In order to minimize cost of maneuvering Vickay-1 space satellite ($\Delta V_1, \Delta V_2, \Delta V_3$) must be applied tangentially in line with the direction of the earth's equator than at the pole, this is because the earth rotates faster with a speed of 1,667 km hr^{-1} at the equator, thus providing the maneuvering process of the satellite with an additional speed of 1,667 km hr^{-1}. This speed bonus means Vickay-1 satellite needs less fuel, low cost, and short time frame for its maneuvering process.

It is worth to note that one of the major contributions of this work lies in the application of Hohmann's function in the context of determining the inclination angle, the total orbit velocity, total orbit period, and total orbit energy of the Vickay-1 space satellite in order to control its orbit against any ionospheric constraints. This is hoped to assist by way of giving space to scientist, meteorologists, militaries, national security agencies, and telecommunication industries afore knowledge of devising means to maximize their space satellite signals amidst ionospheric impact conditions for efficient image resolution and communication.

Conclusions

In this study, we discovered that ionospheric constraint is the major cause of satellite signal fading and multipath over Akure area, thereby resulting into low frequency radio propagation. The geomagnetic constraint was seen to be at strong and extreme conditions at 7.7 Kp and 8.2 Kp, respectively. The highest sunspot count was seen to be 50.4545, while the highest solar flare constraint was observed to be class M having 6.05×10^{-5} watts m^{-2}. The highest CME energy level was seen to be L3 having 6.6572×10^{29} MeV while the fastest solar wind speed observed was 458 km s^{-1}.

Vickay-1 satellites, while operating within the LEO was found to be subjected to sporadic intermittent tracking problem due to increased drag as a result of the strong and extreme geomagnetic storm seen. It was also subjected to memory loss due to the high sunspot count and high radiation storm from the CME. The satellite while in orbit is said to experience radio blackout and radio frequency interference due to the high Class M solar flare constraint and fast solar wind speed observed.

Hence, the need for the maneuvering of Vickay-1 space satellite orbit from LEO to a position between MEO and GEO. The Hohmann's transfer function was used to carry out the maneuvering process from an altitude of approximately 9,583.69 km within the LEO to an altitude of approximately 35,888.53 km between MEO and GEO. This is because the higher the satellite parking altitude, the better the signal coverage. In order to carry out the maneuvering process of the Vickay-1 space satellite, its orbit parameters and that of the Hohmann's transfer orbit parameters must be properly determined, to obtain the exact total orbit velocity, total orbit energy, and total orbit period that would be required.

The technical strength, validity, and limitations of our study were strongly based on the available data; hence, efforts to access the uplink and downlink frequency of the Vickay-1 satellite for valid comparison with modeled signal loss proved abortive due to strong restrictions from its service providers.

Additional Information

Author Contributions

All authors have reviewed the final version to be published and agreed to be accountable for all aspects of the work.

Concept and design: Ajobiewe K. Victor, Sola R. Fayose, Seyi F. Olatoyinbo, Nelson O. Ibigbami

Acquisition, analysis, or interpretation of data: Ajobiewe K. Victor

Drafting of the manuscript: Ajobiewe K. Victor

Critical review of the manuscript for important intellectual content: Ajobiewe K. Victor, Sola R. Fayose, Seyi F. Olatoyinbo, Nelson O. Ibigbami

Supervision: Ajobiewe K. Victor, Sola R. Fayose

Disclosures

Human subjects: All authors have confirmed that this study did not involve human participants or tissue. **Animal subjects:** All authors have confirmed that this study did not involve animal subjects or tissue. **Conflicts of interest:** In compliance with the ICMJE uniform disclosure form, all authors declare the following: **Payment/services info:** All authors have declared that no financial support was received from any organization for the submitted work. **Financial relationships:** All authors have declared that they have no financial relationships at present or within the previous three years with any organizations that might have an interest in the submitted work. **Other relationships:** All authors have declared that there are no other relationships or activities that could appear to have influenced the submitted work.

References

1. Adediji AT, Ismail M, Mandeep JS: Performance analysis of microwave radio refractivity on radio field strength and radio horizon distance over Akure, Nigeria. Wireless Personal Communications. 2014, 79:1893-909. 10.1007/s11277-014-1963-0
2. Adediji AT, Adebusola SO and Ojo JS: Variability of microwave radio refractivity and field strength over some selected locations in Nigeria. Physical Science International Journal. 2017, 14:1-11. 10.9734/psij/2017/33447
3. Agbo GA, Onuorah LO, Okoh D: Contribution of some meteorological parameters in the variation of tropospheric radio refractivity in Yola, Nigeria. EBSU Science Journal. 2020, 1:157-62.

4. Ajileye OO: Long-term average of effective earth radius factor over West Africa using satellite meteorological dataset. International Journal of Electronics Communication and Computer Engineering. 2015, 6:175-79.
5. Akpootu DO, Iliyasu MI: Estimation of tropospheric radio refractivity and its variation with meteorological parameters over Ikeja, Nigeria. Journal of Geography Environment and Earth Science International. 2017, 10:1-12. 10.9734/jgeesi/2017/32534
6. Akpootu DO, Said RS, Mustapha W, Arewa SP, Sulu HT, Iliyasu MI, Salifu SI: Performance analysis of tropospheric radio refractivity on radio field strength and radio horizon distance and its variation with meteorological parameters over Osogbo, Nigeria. International Journal of Advances in Scientific Research and Engineering. 2019, 5:81-97. 10.31695/ijasre.2019.33545
7. Erdős G, Balogh A: Magnetic flux density measured in fast and slow solar wind streams. The Astrophysical Journal. 2012, 753:130. 10.1088/0004-637x/753/2/130
8. Johnson TV, Spohn T: Encyclopedia of the Solar System. Elsevier, Amsterdam; 2014.
9. Victor Nwankwo UJ, Jibiri NN, Dada SS, Onugba AA, Ushie P: Assessment of radio-frequency radiation exposure level from selected mobile base stations (MBS) in Lokoja, Kogi State, Nigeria. Medical Physics. 2012, 10.48550/arXiv.1210.1399
10. Aschwanden MJ, Freeland SL: Automated solar flare statistics in soft X-rays over 37 years of GOES observations: The invariance of self-organized criticality during three solar cycles. The Astrophysical Journal. 2012, 754:112. 10.1088/0004-637x/754/2/112
11. Awan MS, Leitgeb E, Capsoni C, Nebuloni R, Marzuki, Nadeem F, Khan MS: Attenuation Analysis for Optical Wireless Link Measurements under Moderate Continental Fog Conditions at Milan and Graz. 2008 IEEE 68th Vehicular Technology Conference, Calgary, AB, Canada. 2008, 1-5. 10.1109/VETECF.2008.58
12. Ayantunji BG, Okeke PN, Urama JO: Diurnal and seasonal variation of surface refractivity over Nigeria. Progress in Electromagnetics Research B. 2011, 30:201-22. 10.2528/pierb11030902
13. Braeunig RA. Orbital Mechanics. (1997). Accessed: August 12, 2024: http://www.braeunig.us/space/orbmech.htm.
14. Loewe CA, Prölss GW: Classification and mean behavior of magnetic storms. Journal of Geophysical Research Atmospheres. 1997, 102:14209-4213. 10.1029/96ja04020
15. Crane RK: Electromagnetic Wave Propagation through Rain. Wiley-Interscience, New York; 1996.
16. Emmanuel I, Adeyemi B, Adedayo KD: Regional variation of columnar refractivity with meteorological variables from climate monitoring satellite application facility (CM SAF) data over Nigeria. International Journal of the Physical Sciences. 2013, 8:825-34. 10.5897/ijps2013.3852
17. Gallagher PT, Moon YJ, Wang H: Active-region monitoring and flare forecasting-I. Data processing and first results. Solar Physics. 2002, 209:171-83. 10.1023/a:1020950221179
18. Giannattasio F: Ionosphere Monitoring with Remote Sensing. Remote Sensing. 2022, 14:5325. 10.3390/rs14215325
19. Gao J, Brewster K, Xue M: Variation of radio refractivity with respect to moisture and temperature and influence on radar ray path. Advances in Atmospheric Sciences. 2008, 25:1098-113. 10.1007/s00376-008-1098-x
20. Hagino M, Sakurai T, Miyazawa A: Phase relationship between the activity cycles of sunspots and polar faculae. The Solar-B Mission and the Forefront of Solar Physics. 2004, 157.
21. Hassler DM, Dammasch IE, Lemaire P, et al.: Solar wind outflow and the chromospheric magnetic network. Science. 1999, 283:810-13. 10.1126/science.283.5403.810
22. Hudson HS: Solar flares, microflares, nanoflares, and coronal heating. Solar Physics. 1991, 133:357-69. 10.1007/bf00149894
23. Oloketuyi J, Liu Y, Amanambu AC, Zhao M: Responses and periodic variations of cosmic ray intensity and solar wind speed to sunspot numbers. Advances in Astronomy. 2020, 2020:3527570. 10.1155/2020/3527570
24. Harb K: Quality of service improvements in weather impacted satellite communication networks. Carleton University Ottawa. 2010, 3-26.
25. Li KJ, Zhang J, Feng W: Periodicity for 50 yr of daily solar wind velocity. Monthly Notices of the Royal Astronomical Society. 2017, 472:289-94. 10.1093/mnras/stx1904
26. Kallenrode MB: Introduction. Space Physics. Advanced Texts in Physics. Springer, Berlin, Heidelberg; 2001. 10.1007/978-3-662-04443-8_1
27. Lumme E, Pomoell J, Price D, Kilpua EKJ, Kazachenko MD, Fisher GH, Welsch BT: Data-driven, time-dependent modeling of pre-eruptive coronal magnetic field configuration at the periphery of NOAA AR 11726. Astronomy and Astrophysics. 2022, 658:A200. 10.1051/0004-6361/202038744
28. Luhunga PM, Mutayoba E, Masoud H, Chang'a L, Prodanov AD: Analysis of tropospheric radio refractivity over Julius Nyerere International Airport, Dar es Salaam. Space Physics Journal. 2014, 6:21-31.
29. Marcos F, Bowman B, Sheehan R: Accuracy of Earth's thermospheric neutral density models. Paper presented at AIAA 2006-6167, AIAA/AAS Astrodynamics Specialist Conference and Exhibit. Keystone, Colo; 2006. 21-24. 10.2514/6.2006-6167
30. Maltseva OA, Mozhaeva NS, Nikitenko TV: Comparison of model and experimental ionospheric parameters at high latitudes. Advances in Space Research. 2013, 51:599-609. 10.1016/j.asr.2012.04.009
31. Maltseva OA, Mozhaeva NS, Nikitenko TV: Validation of the Neustrelitz Global Model according to the low latitude ionosphere. Advances in Space Research. 2014, 54:463-72. 10.1016/j.asr.2013.11.005
32. McIntosh PS: The classification of sunspot groups. Solar Physics. 1990, 125:251-67. 10.1007/bf00158405
33. McComas DJ, Elliott HA, Schwadron NA, Gosling JT, Skoug RM, Goldstein BE: The three-dimensional solar wind around solar maximum. Geophysical Research Letters. 2003, 30:10.1029/2003gl017136
34. Moreton GE: H-alpha observations of flare-initiated disturbances with velocities ~1000 km/sec. Astronomical Journal. 1960, 65:494. 10.1086/108346
35. Yang X, Zhang HQ, Gao Y, Guo J, Lin GH: A statistical study on photospheric magnetic nonpotentiality of active regions and its relationship with flares during solar cycles 22-23. Solar Physics. 2012, 280:165-81. 10.1007/s11207-012-0061-2
36. Gopalswamy N: Solar Energetic Particle Events and Radio Bursts. Solar and Stellar Astrophysics. 2024, 10.48550/arXiv.2410.08690
37. Oloketuyi J, Liu Y, Zhao M: The periodic and temporal behaviors of solar X-ray flares in Solar Cycles 23 and 24. The Astrophysical Journal. 2019, 874:20. 10.3847/1538-4357/ab064c
38. Mmahi NO, Akinbolati A, Ikechiamaka FN, Akpaneno FA, Joseph E, Ekundayo KR: Studies on surface radio refractivity over some selected cities in north-central, Nigeria. FUDMA Journal of Sciences. 2024, 5:90-99.
39. Pesnell WD, Thompson BJ, Chamberlin PC: The Solar Dynamics Observatory (SDO). Solar Physics. 2011, 275:3-15.
40. Mahrous A, Shaltout M, Beheary MM, Mawad R, Youssef M: CME-flare association during the 23rd solar cycle. Advances in Space Research. 2009, 43:1032-35. 10.1016/j.asr.2009.01.028
41. Rieger E, Share GH, Forrest DJ, Kanbach G, Reppin C, Chupp EL: A 154-day periodicity in the occurrence of hard solar flares?. Nature. 1984, 312:623-25. 10.1038/312623a0

42. Cao JJ, Wu F, Chow JC, et al.: Characterization and source apportionment of atmospheric organic and elemental carbon during fall and winter of 2003 in Xi'an, China. Atmospheric Chemistry and Physics. 2005, 5:3127-137. 10.5194/acp-5-3127-2005
43. Shen Y, Liu Y, Tian Z, Qu Z: On a small-scale EUV wave: the driving mechanism and the associated oscillating filament. The Astrophysical Journal. 2017, 851:101. 10.3847/1538-4357/aa9af0
44. Shen Y, Zhou X, Duan Y, Tang Z, Zhou C, Tan S: Coronal quasi-periodic fast-mode propagating wave trains. Solar Physics. 2022, 297:20. 10.1007/s11207-022-01953-2
45. Owens SR, Macdonald M: An extension and numerical analysis of the Hohmann spiral transfer. 63rd International Astronautical Congress. 2012,
46. Suess S: Overview and Current Knowledge of the Solar Wind and the Corona. The Solar Probe. NASA/Marshall Space Flight Center. 1999, 2:4-9.
47. Schulz W: Walter Hohmann's contributions towards space flight: an appreciation on the occasion of the centenary of his birthday. Acta Astronautica. 1980, 7:1213-227. 10.1016/0094-5765(80)90001-6
48. Khanna R: Call for applications for two Editor-in-Chief positions of Astrophysics and Space Science (Ap&SS). Astrophysics and Space Science. 2013, 346:1. 10.1007/s10509-013-1490-6
49. Zirker JB: Coronal holes and high-speed wind streams. Reviews of Geophysics. 1977, 15:257-69. 10.1029/rg015i003p00257
50. Žilinskas M, Tamošiunas S, Tamošiūnaitė M, Tamošiūnienė M: Yearly, seasonal and daily variations of radio refractivity. Acta Physica Polonica A. 2011, 119:533-36.
51. Wang YM, Ye PZ, Wang S, Zhou GP, Wang JX: A statistical study on the geoeffectiveness of Earth-directed coronal mass ejections from March 1997 to December 2000. Journal of Geophysical Research Atmospheres. 2002, 107:SSH 2-1-SSH 2-9. 10.1029/2002ja009244
52. Ajewole MO, Oyedum OD, Adediji AT, Moses AS, Eiche JO: Spatial Variability of VHF/UHF Electric Field Strength in Niger State, Nigeria. International Journal of Digital Information and Wireless Communications (IJDIWC); Society of Digital Information and Wireless Communications. 2013, 3:29.
53. Bain HM, Steenburgh RA, Onsager TG, Stitely EM: A summary of national oceanic and atmospheric administration space weather prediction center proton event forecast performance and skill. Space Weather. 2021, 19:e2020SW002670. 10.1029/2020sw002670